physchem

MDPI

Article

The Modeling of Perovskite Materials $CsPbX_3$ (X = I, Br) by Changing the Concentration of Halide: Experimental and DFT Study

Alicja Mikłas [1,2], Zbigniew Starowicz [3], Marek Lipiński [3], Marek J. Wójcik [1,4], Takahito Nakajima [4] and Mateusz Z. Brela [1,4,*]

1 Faculty of Chemistry, Jagiellonian University, Gronostajowa 2, 30-387 Kraków, Poland
2 Doctoral School of Exact and Natural Sciences, Jagiellonian University, Prof. S. Łojasiewicza 11, 30-348 Kraków, Poland
3 Institute of Metallurgy and Materials Science, Polish Academy of Science, Reymonta 25, 30-059 Kraków, Poland
4 Institute of Physical and Chemical Research (RIKEN), Center for Computational Science, 7-1-26, Minatojima-Minami-Machi, Chuo-ku, Kobe 650-0047, Hyogo, Japan
* Correspondence: brela@chemia.uj.edu.pl

Abstract: In recent years, perovskites have quickly gained popularity in applications related to photonic devices and in photovoltaic applications. Over the last several years, the efficiency of photovoltaic (PV) cells based on perovskites has matched the efficiency of PV cells based on silicon. $CsPbBr_3$ perovskite is gaining more and more popularity, but due to the too large band gap value, its use in photovoltaics is difficult. Another perovskite, very intensively researched and giving hope for further development of photovoltaics, is $CsPbI_3$. The $CsPbI_3$ band gap is smaller than the $CsPbBr_3$ band gap and more suitable for photovoltaic applications. However, $CsPbI_3$ is unstable under the conditions of solar cell operation. To reduce the band gap value and increase the perovskite stability, very intensive research, both theoretical and experimental, is devoted to structures with mixed halides, i.e., a mixture of bromine and iodine with the general formula $CsPbBr_xI_{3-x}$. Computational methods based on DFT have been successfully used for many years to determine the parameters and properties of materials. The use of computational methods significantly reduces the costs of the research performed compared to experimental techniques. The aim of this work is to understand the band gap changes based on DFT calculations as well as XRD and UV-Vis experiments for $CsPbBr_3$, $CsPbI_3$, and $CsPbBr_xI_{3x}$ perovskites.

Keywords: perovskites; DFT; band gap; XRD; UV-Vis

Academic Editor: José Solla Gullón

Received: 15 October 2024
Revised: 14 November 2024
Accepted: 26 November 2024
Published: 7 January 2025

Citation: Mikłas, A.; Starowicz, Z.; Lipiński, M.; Wójcik, M.J.; Nakajima, T.; Brela, M.Z. The Modeling of Perovskite Materials $CsPbX_3$ (X = I, Br) by Changing the Concentration of Halide: Experimental and DFT Study. *Physchem* **2025**, *5*, 3. https://doi.org/10.3390/physchem5010003

1. Introduction

Over the past decades, the world's energy consumption has grown significantly and continues to do so. Due to that, new and alternative energy sources are being developed. One of the most intensively developed alternative energy sources is photovoltaics [1,2]. Nowadays, the best-known and commonly applied technique for building photovoltaic cells (PVCs) is technology based on silicon [3]. However, due to opinions that silicon PV cells have reached their maximal efficiency, new alternative materials to replace silicon are being searched for [4,5]. A group of materials that offers the possibility for the further development of photovoltaics and for replacing silicon is perovskites.

Perovskites are a class of compounds with a general formula ABX_3. In ABX_3, A stands for cation located in the vertex of the face-centered cubic lattice (e.g., NH_4^+, $C_3H_3^+$,

and $CH_3NH_3^+$, [6]), B for metal cation (e.g., Pb^{2+}, Sn^{2+}, etc.), and X for halogen anion or the coexistence of several halogens (Cl^-, Br^-, and I^-) [6,7] placed in the core and apex of the octahedra. These metal halide octahedra are bonded together and form a stable three-dimensional structure. Thanks to crystallographic structure, perovskites exhibit many properties desired in photovoltaics, such as low exciton binding energy and high absorption coefficients, outstanding low exciton binding energy, and high optical absorption coefficients. Also, perovskites possess large dielectric constant, which makes electrons and holes possible to collect and transmit. Depending on composition, perovskites exhibit various crystallographic structures. The formula that is used to predict the formation of perovskite structure depending on its composition is the Goldschmidt factor t [8–10] given by the following equation:

$$t = \frac{r_A + r_x}{\sqrt{2}(r_B + r_x)} \quad (1)$$

where r_A, r_B, and r_x stand for the ionic radii of A, B, and x, respectively. Generally, a perovskite structure can be formed when the Goldschmidt parameter is between 0.8 and 1. However, for t lower than 0.8, the perovskite structure will be formed but distorted because of BX_3 tilting. When considering the type of A cations, on the other hand, if t is greater than 1, the A cation is too large to form a perovskite structure, and if t is smaller than 0.8, the A cation is too small to form a perovskite.

The perovskites investigated in this paper have a general composition of $CsPbBr_xI_{3-x}$. However, the initial structures were $CsPbBr_3$ and $CsPbI_3$. $CsPbBr_3$ and $CsPbI_3$ expose different crystallographic structures [6,9,11]. The chemical composition of perovskite influences the electronic structure of a material, and so the shape and course of valence band maximum (VBM), conductance band minimum (CBM), and band gap value (E_g) [11,12]. $CsPbBr_3$ and $CsPbI_3$ occur in several polymorphs stable in different temperature ranges. The polymorph that can be applied in PVCs, for both $CsPbBr_3$ and $CsPbI_3$, is cubic. Cubic $CsPbBr_3$ is more stable at room temperature than cubic $CsPbI_3$ but has a too large band gap value to be applied in PVCs. The band gap value of $CsPbI_3$ is more appropriate for PVCs than the $CsPbBr_3$ band gap value. To increase perovskite durability and adjust band gap value, mixed halide $CsPbBr_{3-x}I_x$ perovskites are developed. With a bromine content in $CsPbBr_{3-x}I_x$ the material thermodynamic stability increases, while iodine addition reduces band gap value [7,11–14].

This paper focuses on the analysis of $CsPbBr_{3-x}I_x$ perovskites. The paper consists of two parts—experimental and computational. The main subject of both parts of the paper is to study the effect of iodine dopant in a unit cell on unit cell parameters, crystal morphology, band gap value, and state density.

2. Materials and Methods

2.1. Experimental Details

Two series of samples with various PbI_2 concentrations, so $10PbI_2$ and $20PbI_2$, in a $PbBr_2$ + PbI_2 mixture, were prepared. All the samples were prepared with the spin coating method. The samples were prepared by applying two layers: the first layer was a mixture of $PbBr_2$ + PbI_2, and the second was CsBr. The influence of PbI_2 concentration on the crystallization process, appearance of the perovskite phase, its degradation, and band gap values was investigated. The investigated samples were prepared by applying subsequent layers and annealing. All the layers were applied on glass slides with FTO (Fluorine-doped Tin Oxide) on them.

The first layer was 1 M solutions of $PbBr_2$ + PbI_2 with DMSO as a solvent. The substratres were preheated for 120 °C and the solution stayed at room temperature. The deposition was conducted by spin coating at 2500 r.p.m. for 25 s. The samples with a

$PbBr_2$ + PbI_2 layer were annealed for 30 min on a hotplate at 120 °C. After the $PbBr_2$ + PbI_2 layer, CsBr layers were applied. For $PbBr_2$ + PbI_2, only one layer is needed, while for CsBr several layers are needed because the goal of applying CsBr layers is to convert initial non-perovskite phases to a perovskite phase. The number of CsBr layers must be appropriately selected, depending on the PbI_2 concentration in a sample, to achieve a complete transition to the perovskite phase and prevent them from occurring in Cs-rich phase. CsBr layers were also deposited with the spin coating method and then annealed. CsBr solution had a concentration of 0.07 M, and methanol was used as a solvent. Each subsequent CsBr layer was annealed for 5 min at 250 °C on a hotplate.

To characterize the samples an SEM analysis was performed, and XRD measurements and UV-Vis spectra were measured. The XRD measurements of the perovskite films were carried out using a Bruker D8 Discover diffractometer equipped with a Cu K_α X-ray source. Bragg–Brentano (θ–2θ) X-ray diffraction continuous scans were performed over the range of 2θ = 10–100° at 2 s per step with a step size of 0.02°. The transmittance and reflectance of the perovskite films were measured using an optical spectrophotometer (Lambda 950S, Perkin Elmer, Waltham, MA, USA). The band gap of the perovskite films was calculated by Tauc's plot, which uses the values of the absorption coefficient α of the film calculated from the transmittance (T) and reflectance (R) data according to the following formula:

$$\alpha = -\frac{1}{d} \times ln\left[\frac{T}{(1-R)}\right] \quad (2)$$

We used the reflectance data in order to increase accuracy.

2.2. Computational Details

The second part focuses on the analysis of the structural and electronic properties of $CsPbBr_{3-x}I_x$. For the structural properties, the focus was on the influence of halides on *a*, *b*, and *c* parameters and unit cell volume. For the electronic properties, the influence of iodine concentration on the band gap value and CBM/VBM was investigated.

The structural and electronic properties of $CsPbBr_{3-x}I_{xx}$ have been theoretically examined using the density functional theory (DFT) with Perdew–Burke–Ernzerhof generalized gradient approximation (PBE-GGA) [15] as well as the dispersive correction of vdW interactions D3 Grimme [16]. The mixed wave base DZVP-MOLOPT-SR-GTH with plane waves and pseudopotential GTH-PBE have been applied in the cp2k code [17,18]. The cutoff kinetic energy was set to 700 Ry.

3. Results and Discussion

3.1. Experimental Part

The goal of applying CsBr layers on $PbBr_2$ + PbI_2 layers is to convert the initial phases to perovskite phase $CsPbBr_{3-x}I_x$. The number of applied CsBr layers must be appropriately selected depending on the PbI_2 concentration in samples. Too few CsBr layers will not convert the initial phases to a perovskite phase resulting in Cr deficient $CsPb_2Br_5$ phase, while too many CsBr layers will cause the perovskite phase to change into a cesium-rich, Cs_4PbBr_6 non-perovskite phase.

Below, the analysis of the SEM pictures and XRD patterns investigate the influence of subsequently applied CsBr layers and the optimal number of layers depending on PbI_2 concentration. The conclusions from the analysis of the SEM images and XRD patterns are then compared with the results of the UV-Vis measurements.

3.2. Analysis of SEM Images

Figures 1–4 represent the SEM images of $PbBr_2$ + PbI_2 with various PbI_2 concentrations with 1.5 k and 10 k zoom. Moreover, Figures 1 and 2 present $PbBr_2$ + 10% PbI_2 with six subsequent CsBr layers whereas Figures 3 and 4 present $PbBr_2$ + 20% PbI_2 with five subsequent CsBr layers. Images with a focus of 1.5 k allow for the analysis of large fragments of the sample, while images with a focus of 10 k enable a thorough analysis of the crystal morphology.

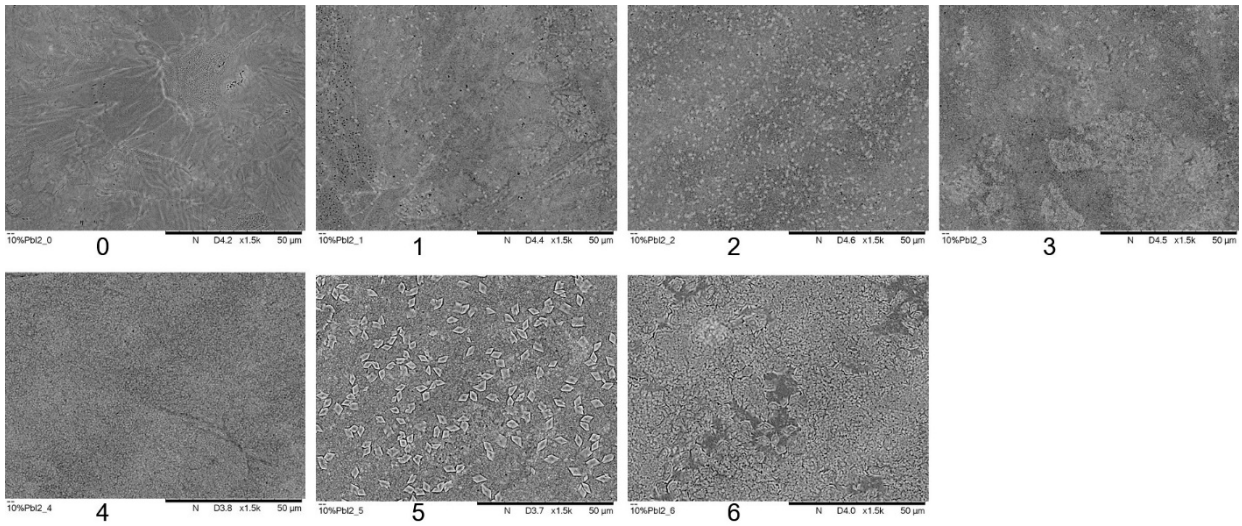

Figure 1. SEM of PbBr2 with 10% PbI_2 and after susecquent *CsBr* layers with 1.5 k magnification. Numbers 0–6 stand for subsequent CsBr layers, so 0: no CsBr layers, 1: one CsBr layer, 2: two CsBr layers, 3: three CsBr layers, 4: four CsBr layers, 5: five CsBr layers, 6: six CsBr layers.

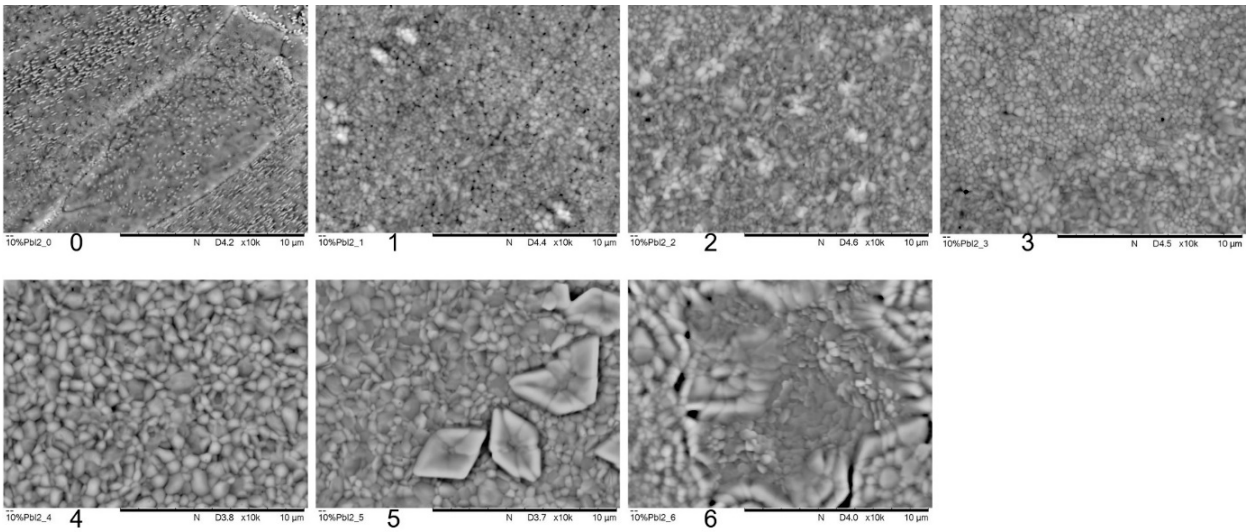

Figure 2. SEM of PbBr2 with 10% PbI_2 (0) and after susecquent *CsBr* layers (1–6) with 10k magnification. Numbers 0–6 stand for subsequent CsBr layers, so 0: no CsBr layers, 1: one CsBr layer, 2: two CsBr layers, 3: three CsBr layers, 4: four CsBr layers, 5: five CsBr layers, 6: six CsBr layers.

For the $10PbI_2$ sample (zoom 10 k, Figure 2) after applying the fourth CsBr layer, crystals of a size comparable to the crystals of $20PbI_2$ and the third CsBr layer start to appear. The application of the fifth CsBr layer causes further crystal growth, while also the cesium-rich, Cs_4PbBr_6 phase appears. After applying the sixth CsBr layer, crystal degradation contines as more of this phase covers the surfaces of prevovskite phase underneath.

For the SEM pictures of the 20PbI_2 samples (zoom 10 k, Figure 4), for the third CsBr layer, well-formed crystals with a size of about 10 µm are observed. For the fourth CsBr layer, further crystal growth is observed. However, in the case of 20PbI_2 samples the is tencendy of formation of Cs rich phase in random location.

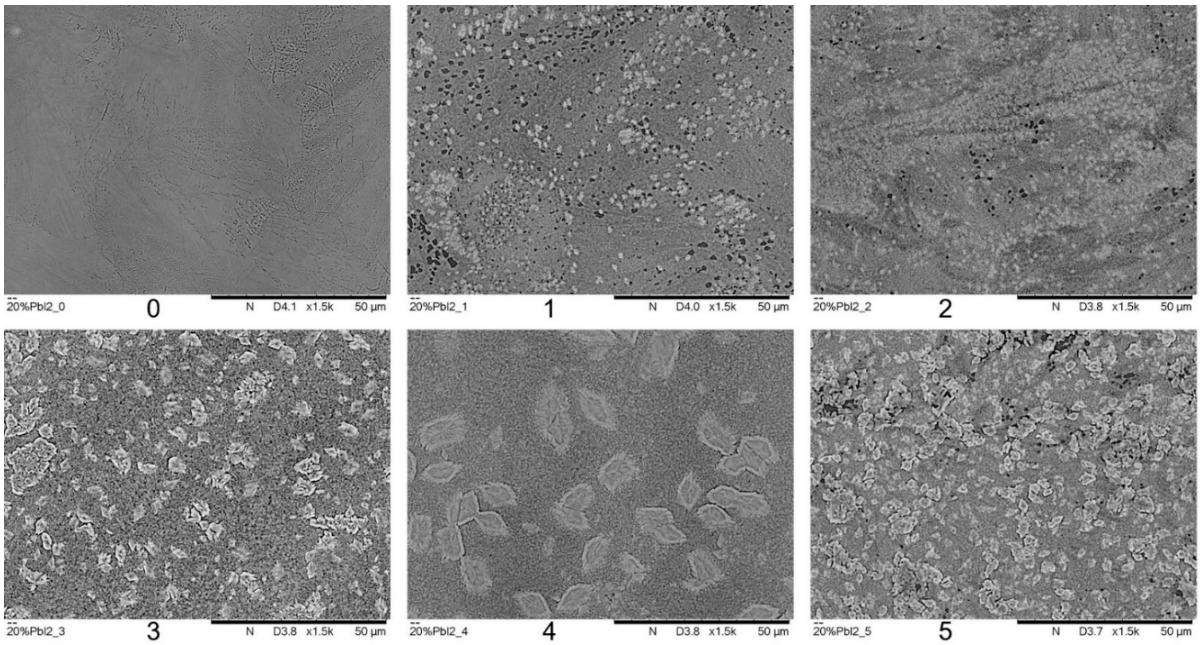

Figure 3. SEM of PbBr2 with 20% PbI_2 (0) and after susecquent *CsBr* layers (1–5) with 1.5 k magnification. Numbers 0–5 stand for subsequent CsBr layers, so 0: no CsBr layers, 1: one CsBr layer, 2: two CsBr layers, 3: three CsBr layers, 4: four CsBr layers, 5: five CsBr layers.

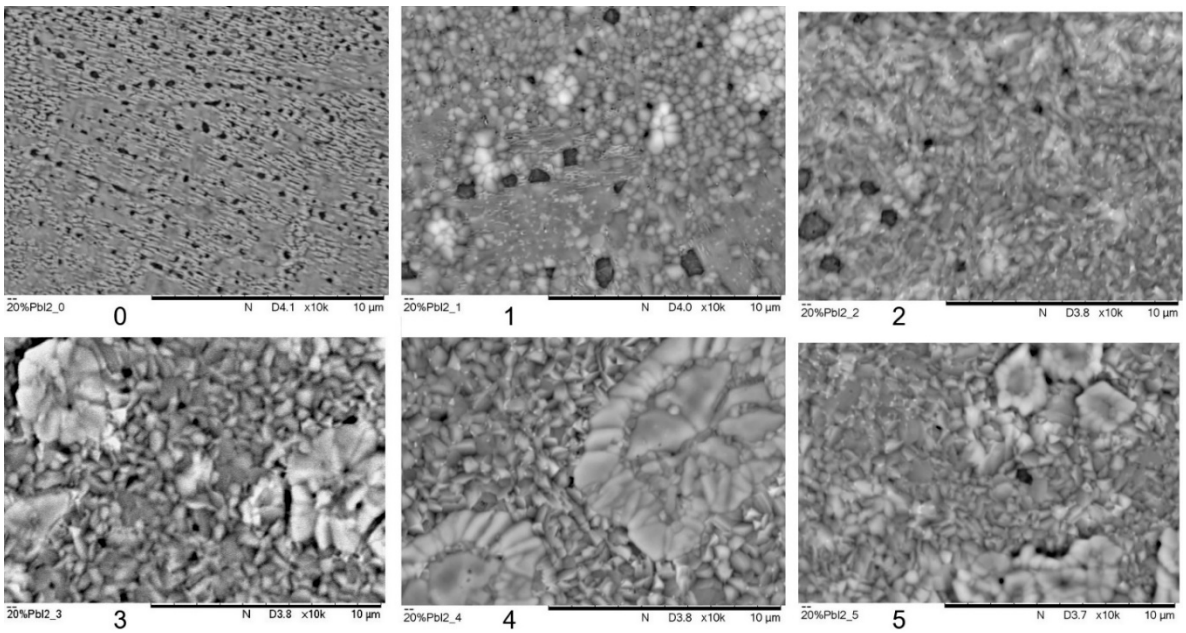

Figure 4. SEM of PbBr2 with 20% PbI_2 (0) and after susecquent *CsBr* layers (1–5) with 10k magnification. Numbers 0–5 stand for subsequent CsBr layers, so 0: no CsBr layers, 1: one CsBr layer, 2: two CsBr layers, 3: three CsBr layers, 4: four CsBr layers, 5: five CsBr layers.

3.3. Analysis of XRD Patterns

Based on specific signals in the XRD spectra, it is possible to determine the influence of CsBr layers on crystallization and the presence of phases in the tested samples.

By analyzing the XRD patterns in Figures 5 and 6, it may be found that depending on the PbI_2 concentration, a different number of CsBr layers is necessary for the transition of the initial phase to the perovskite phase. The most noticeable difference when comparing the two diffractograms is for the third CsBr layer.

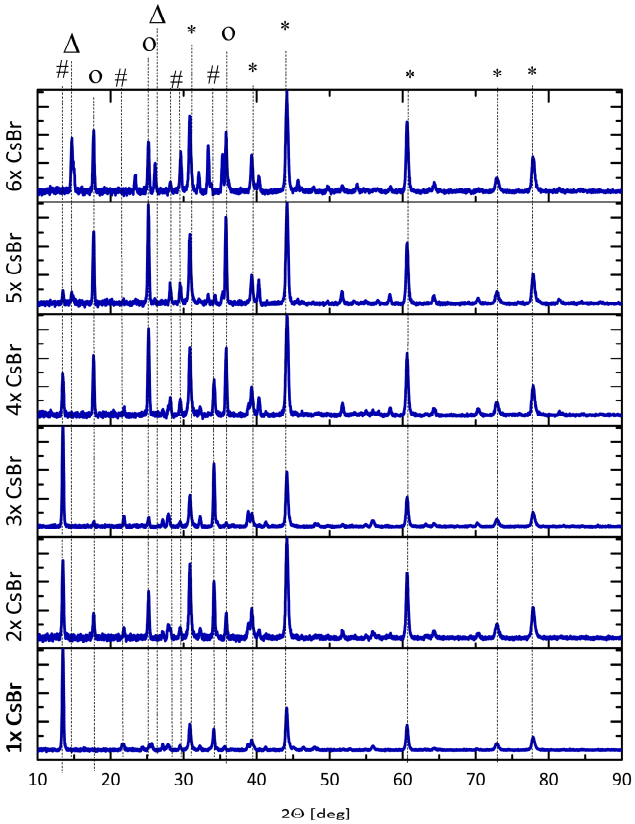

Figure 5. XRD pattern for $10PbI_2$ with subsequent CsBr layers (from single layer to 6 CsBr layers). Symbols: *—FTO, #—$CsPb_2Br_5$, o—$CsPbBr_3$, Δ—Cs_4PbBr_6.

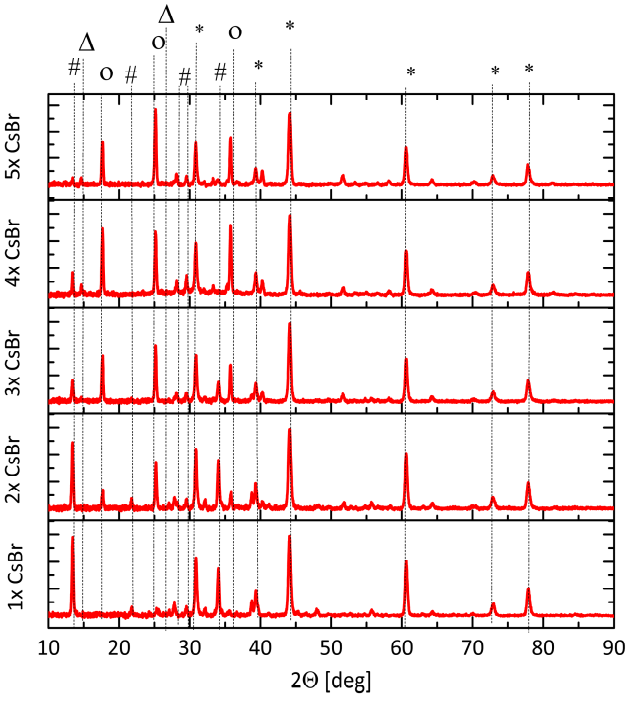

Figure 6. XRD pattern for $20PbI_2$ with subsequent CsBr layers (from single layer to 5 CsBr layers). Symbols: *—FTO, #—$CsPb_2Br_5$, o—$CsPbBr_3$, Δ—Cs_4PbBr_6.

When it comes to 10PbI_2 series, based on the XRD pattern in Figure 5, it may be noticed that the perovskite phase appears for the fourth CsBr layer and its further growth may be noticed for the fifth CsBr layer. For the sixth CsBr layer, non-perovskite, Cs reaches too high concettation and the perovskite phase decomposes precipitating the Cs_4PbBr_6 phase.

For 20PbI_2, according to the XRD patterns in Figure 6, the perovskite $CsPbBr_3$ phase appears after applying the third CsBr layer and further growth may be noticed for the fourth CsBr layer. The degradation of the perovskite phase and appearance of the Cs_4PbBr_6 layer starts after applying the fifth CsBr layer.

For the 10 Pb_{I2} and 20PbI_2 samples, the growth of the perovskite phase for subsequent layers is possible to observe through the increase in the intensity of peaks on the XRD patterns. The degradation of the perovskite phase and growth of the Cs reach phase can be observed by increasing the ratio of the intensities of peaks from the perovskite phase to the intensity of peaks from the Cs reach phase.

3.4. Transmittance Plots

The transmittance UV-Vis spectroscopy plots presented in Figures 7 and 8 may be used to detect and confirm the existence of the perovskite phase in the investigated sample and support the results of the XRD analysis. The plots in Figures 7 and 8 present the transmittance UV-Vis spectra as a function of wavelength of the samples 10PbI_2 and 20PbI_2 with subsequent CsBr layers. The presence of the perovskite phase is manifested by a significant decrease in transmittance (plots 7a and 8a). Based on plots presenting the minimal values of transmittance at around 515 nm from Figures 7b and 8b as a function of several applied CsBr layers (Figures 7b and 8b), the highest share of the perovskite phase may be confirmed. The most uniform perovskite phase is considered to be the phase for the CsBr layer, for which the first point in the series of minima is observed in diagrams 7b and 8b.

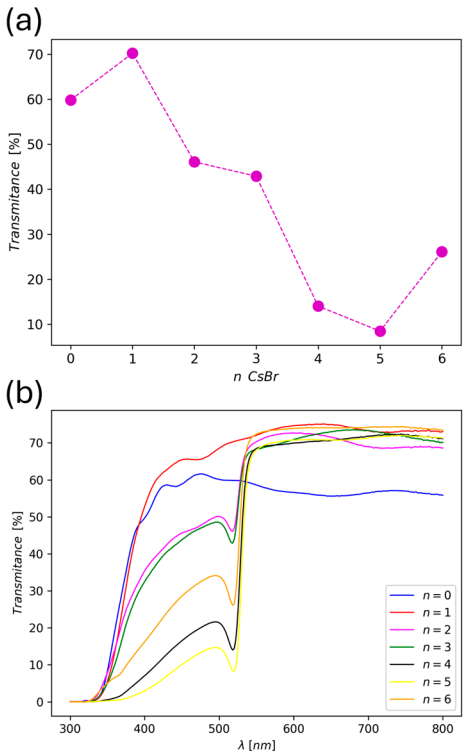

Figure 7. Data for determining phase transitions for $PbBr_2$ + 10PbI_2. (**a**) Transmittance as a function of wavelength for samples with successive (0–6) CsBr layers for 10% PbI_2 content. (**b**) transmittance minimum for λ = 518 nm as a function of successive (0–6) CsBr layers for 10% PbI_2 content.

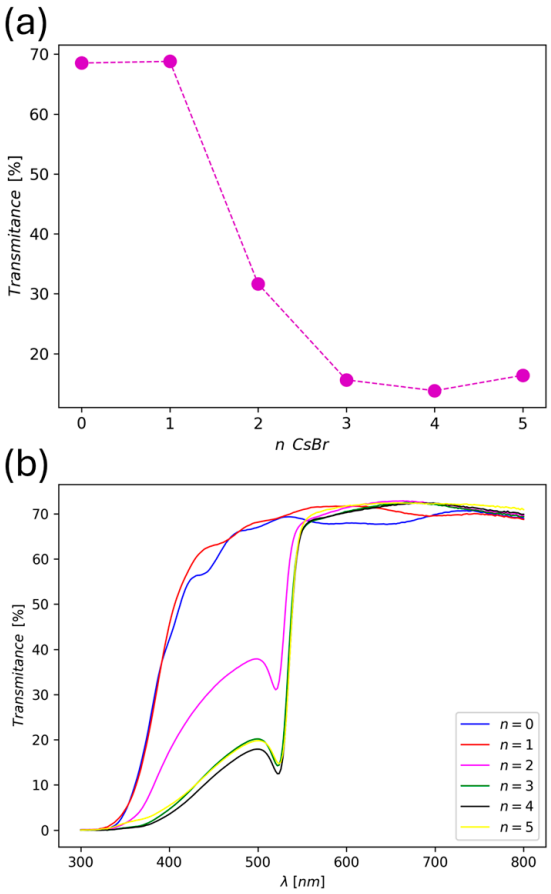

Figure 8. Data for determining phase transitions for $PbBr_2$ + 20PbI_2. (**a**) Transmittance as a function of wavelength for samples with successive (0–5) CsBr layers for 20% PbI_2 content. (**b**) transmittance minimum for λ = 518 nm as a function of successive (0–5) CsBr layers for 20% PbI_2 content.

By analyzing Figures 7 and 8, it may be noticed that for the 10PbI_2 and 20PbI_2 sample, the perovskite phase appears after applying the second CsBr layer, however highest share of perovskite phase is after applying the fifth CsBr layer for 10PbI_2 and fourth for 20PbI_2. Judging by the further increase in transmittance in both Figures when another CsBr layer is added, perovskite becomes ovestatureated with Cs decomposes precipitating Cs_4PbBr_6 phase. after applying the sixth CsBr layer.

Rapid decrease in transmittance as a function of the applied CsBr layers indicates phase transition from the non-perovskite to perovskite abrsorbing phase of a compound with the same chemical composition. Moreover, the minimal value of transmittance as a function of applied CsBr layers indicates the highest share of perovskite phase. Additionaly, Cs-rich nonabsorbing phase (Cs_4PbBr_6) that coexists with the perovskite phase causes the increase of transmittance. For sample 10PbI_2, a rapid decrease in transmittance is observed after applying the third CsBr layer (Figure 7a), whereas a minimal value of transmittance is observed for the fifth CsBr layer (Figure 7a). When it comes to the 20PbI_2 samples, a rapid decrease in transmittance is observed after applying the second CsBr layer (Figure 8a), whereas a minimal value of transmittance is observed for the fourth CsBr layer (Figure 8a). When comparing Figures 7a and 8a, it may also be observed that for Figure 7a, sample 10PbI_2, the decrease in transmittance values is distorted compared to the same trend but for Figure 8a, sample 20PbI_2. This may be due to the worse quality of 10PbI_2 than 20PbI_2. The XRD patterns for 10PbI_2 (Figure 5) and 20PbI_2 (Figure 6) confirm the presence of a Cs-rich phase for both lines of samples.

3.5. Band Gap Analysis

Based on the UV-Vis spectra, using the Tauc method, the band gap value was determined for samples with different PbI_2 concentrations. E_g values from Figure 9a as a function of the PbI_2 content in the unit cell are shown in Figure 9b. Based on Figure 9b, it can be seen that with the increase in the content of PbI_2 in the unit cell, the value of the energy gap decreases compared with Table 1. This relationship is in line with the expectations and literature values [13,14].

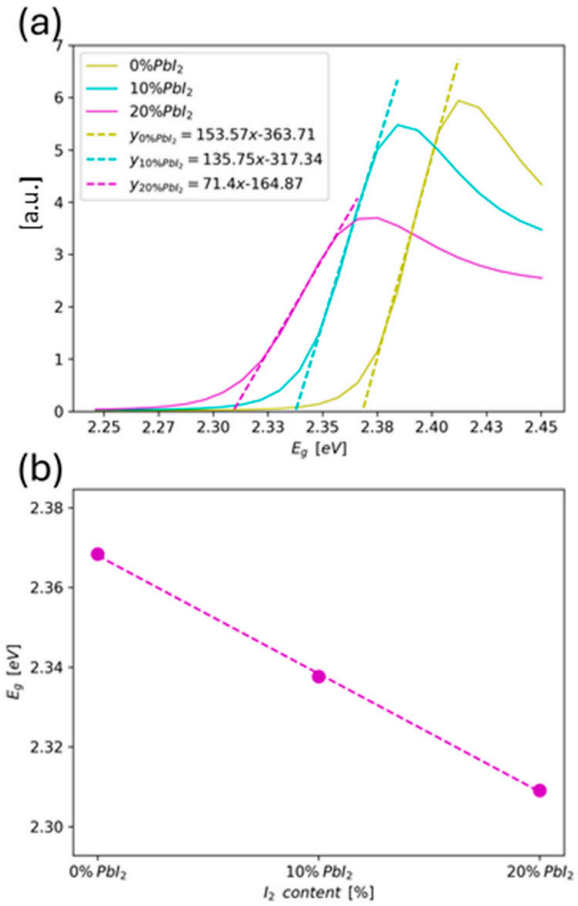

Figure 9. Data for band gap values. (**a**) Fragments of the UV-VIS spectra to determine band gap; (**b**) band gap values as a function of iodine concentration in the unit cell.

Table 1. Band gap values with iodine content in unit cell.

PbI_2 Concentration [%]	Eg [eV]
0	2.368
10	2.338
20	2.309

3.6. Summary of Experimental Part

After analyzing the SEM pictures and XRD patterns of the samples with 10% and 20% PbI_2 concentration and subsequently added CsBr layers, it may be noticed that depending on PbI_2 concentration, the different number of CsBr layers is necessary for a $CsPbX_3$ perovskite phase to appear. According to the XRD patterns, the lower the PbI_2 concentration is, the more CsBr layers are needed to convert the initial phase to the $CsPbX_3$ phase. The optimal number of CsBr layers for the $10PbI_2$ samples is five, and for $20PbI_2$ samples is four. For the next deposited layer, for $10PbI_2$ and $20PbI_2$, the decomposition of the perovskite layer was observed, and the appearance of a non-perovskite layer rich in cesium. The

results from the SEM pictures and XRD were compared with the UV-Vis spectroscopy results. The conclusions from the UV-Vis measurements confirm the conclusions from the SEM/XRD measurements. For the 10PbI_2 sample, the perovskite phase appears for the second deposited CsBr layer, is most uniform for the fifth CsBr layer,. On the other hand, for the 20PbI_2 sample, the perovskite phase appears for the second deposited CsBr layer, is most uniform for the fourth CsBr layer, and disappears for the fifth CsBr layer.

3.7. Computational Part

All the calculations were performed for two input structures, so $CsPbBr_3$* and $CsPbI_3$*. The initial structures were gradually substituted with iodine or bromine, respectively. The input structures are marked with an asterisk. Figure 10 presents structures of $CsPbBr_3$ and Figure 11 presents structures of $CsPbI_3$.

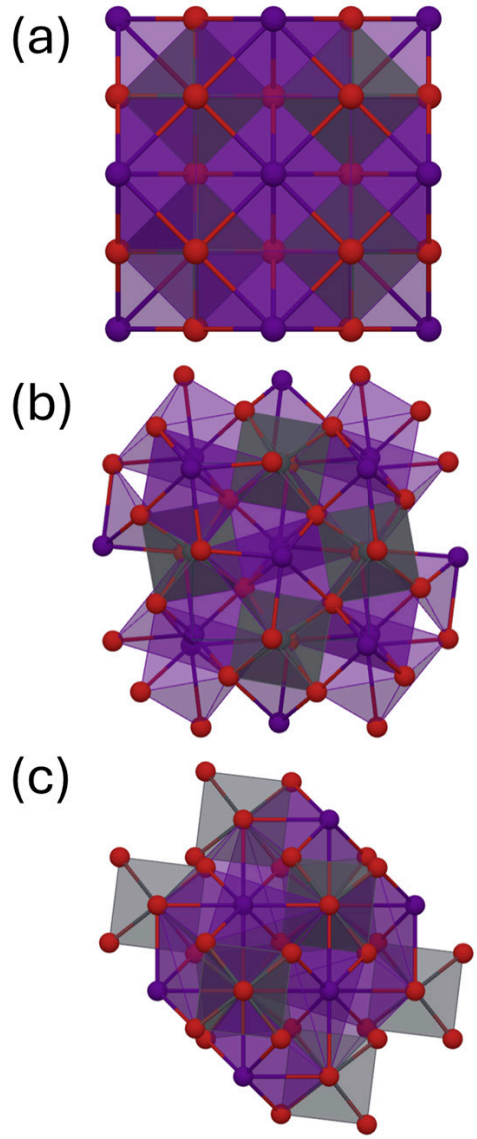

Figure 10. $CsPbBr_3$ polymorphs: (**a**) cubic; (**b**) orthorhombic; (**c**) tetragonal.

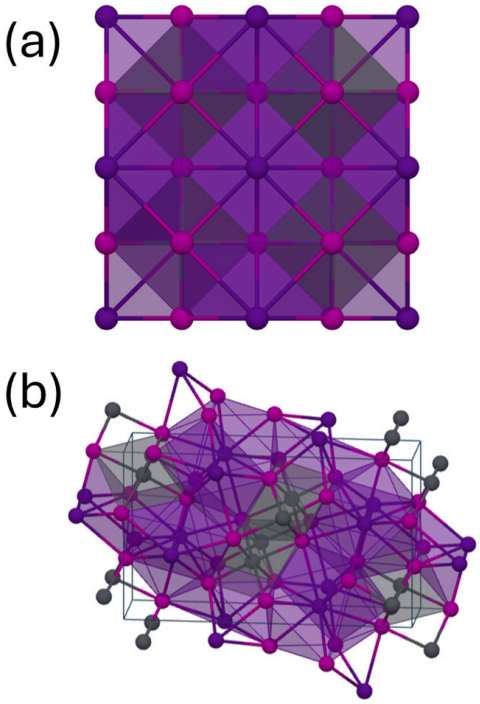

Figure 11. $CsPbI_3$ polymorphs: (**a**) cubic; (**b**) orthorhombic.

For both $CsPbBr_3$ and $CsPbI_3$, calculations were performed for all the polymorphs: cubic, orthorhombic, and tetragonal for $CsPbBr_3$ (Figure 10) and cubic and orthorhombic for $CsPbI_3$ (Figure 11). The results presented in the paper are for $CsPbBr_3$ cubic and $CsPbI_3$ cubic. The initial structures for $CsPbBr_3$ and $CsPbI_3$ are gradually substituted with another halide until the halide is completely replaced with another. Replacing halides in the input structures goes according to paths below:

$CsPbBr_3$ as initial structures:

$$CsPbBr_3{}^* \rightarrow CsPbBr_2I \rightarrow CsPbBrI_2 \rightarrow CsPbI_3$$

$CsPbI_3$ as initial structures:

$$CsPbI_3{}^* \rightarrow CsPbI_2Br \rightarrow CsPbIBr_2 \rightarrow CsPbBr_3$$

3.8. Influence of Chemical Composition on Unit Cell Parameters

Figure 12 presents the calculated unit cell parameters a, b, and c, and unit cell volume V for the initial and transition structures with various bromine and iodine concentrations. When analyzing Figure 3, it may be noticed that with increasing iodine concentration in the unit cell, unit cell parameters a, b, and c, and unit cell volume *V* increase. It should be pointed out that iodine has a larger radius than bromine, so when iodine atoms are incorporated into perovskite crystals, the a, b, and c periods should increase. This trend is observed in Figure 12. For Figure 12a, the starting structure is $CsPbI_3{}^*$ subsequently substituted with Br atoms to achieve $CsPbBr_3$, whereas for Figure 12b starting structure is $CsPbBr_3{}^*$ subsequently substituted with I atoms to achieve $CsPbI_3$. Starting structures from the experimental data are marked with a star ($CsPbI_3{}^*$ and $CsPbBr_3{}^*$), whereas structures with the same composition, but generated by substituting experimental, so initial structures with bromine or iodine, are not marked with a star ($CsPbI_3$ and $CsPbBr_3$). Both panels in Figure 12 (so panels a and b) present how periods a, b, and c and unit cell volume V change depending on perovskite composition. For both panels in Figure 12, the periods and unit cell volume change when changing perovskite composition. While there is no clear trend observed in how period values change, there is a relatively clear trend for a

change in unit cell volume. Moreover, the analysis of unit cell volume is claimed to be more reliable than the analysis of every period separately. For both panels in Figure 12, with an increase in iodine concentration, unit cell volume also increases. This trend is expected and observed. However, there is some difference in this trend for the two panels. For panel b, the trend is slightly distorted compared to panel a. This is most likely due to the fact that in panel b, the initial structure is clear bromine ($CsPbBr_3$*) and initial periods a, b, and c are smaller than the initial periods for the initial structure clear iodine ($CsPbI_3$*) and when adding bigger atoms (which is iodine) to crystals with smaller atoms (which is bromine) and smaller periods, crystal may become distorted. Most likely, such distortion, being a result of adding bigger atoms to a crystal with smaller atoms and periods, is reflected as a deviation from the observed trend, so there is an increase in unit cell volume with an increase in iodine concentration.

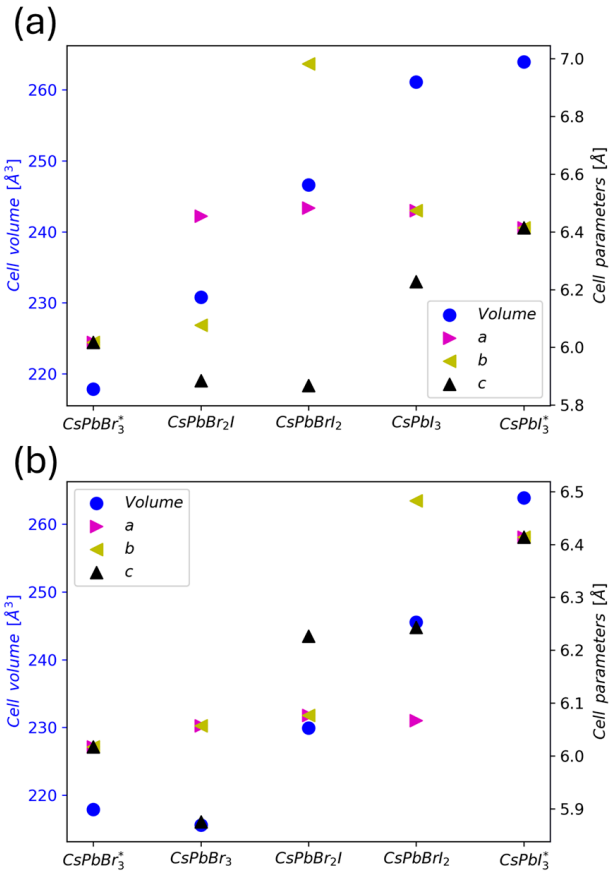

Figure 12. Calculated cell parameters and cell volume; panel (**a**) represents the achieved structures obtained from the starting point: cubic $CsPbI_3$, panel (**b**) shows the achieved structures obtained from the starting point: cubic $CsPbBr_3$.

3.9. Density of States

To understand the origins of the bang gap decreasing with the iodide concentration, the analysis of the Density of States has been performed. Firstly, the addition of iodide to the structure dramatically changes the number of states involved in the valence band maximum. The position of the VBM shifts to higher energy (compare the panels in Figure 13). The position of the CBM does not move so much because the origin of this band is orbitals from the lead. However, for the $CsPbBr_2I$ structure, the conductance band reflects the two picks, both originating from lead orbitals. When analyzing DOS plots, it may be noticed that the band gap value changes with increasing iodine concentration in the unit cell. As the concentration of iodine increases, the band gap value decreases.

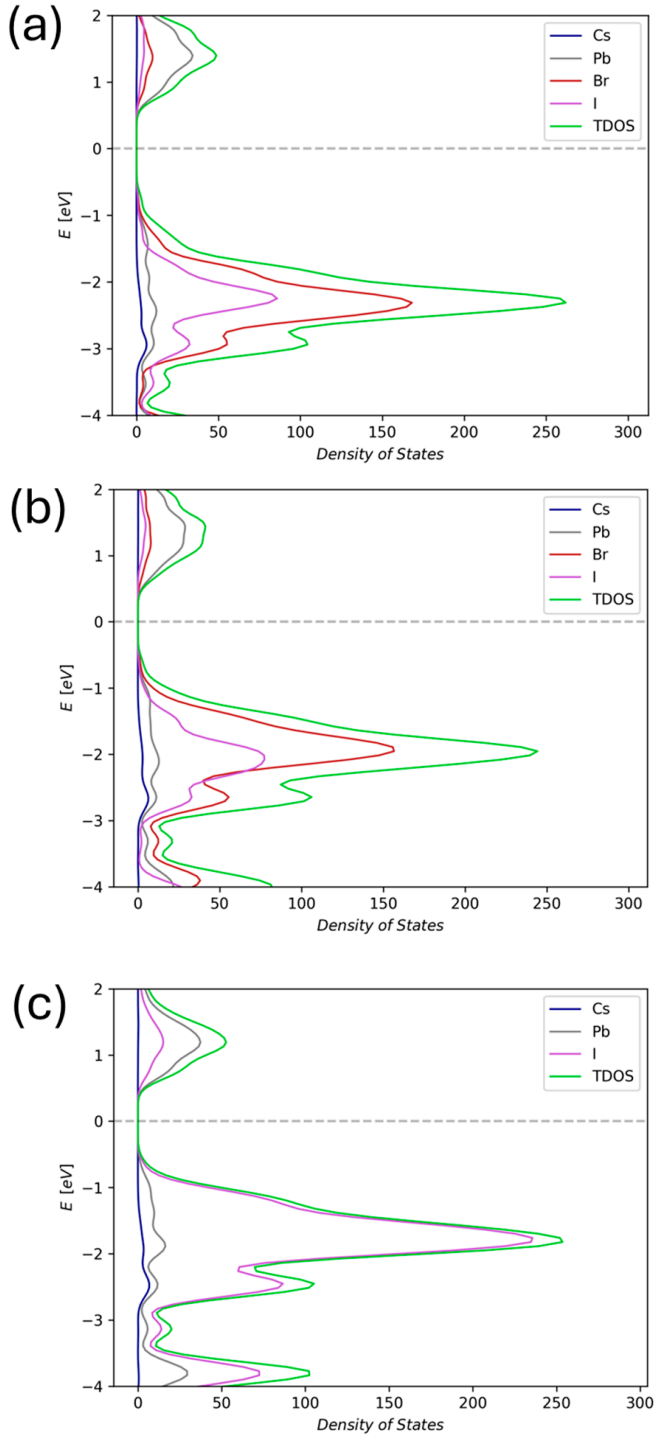

Figure 13. The Density of States for the calculated structure using the protocol with starting point as a cubic structure of $CsPbI_3$: (**a**) $CsPbBr_2I$; (**b**) $CsPbBrI_2$; (**c**) $CsPbI_3$.

In addition, the calculations for the crystallographic and the calculated structures have been performed. The results are depicted in Figure 14, and the second pathways of calculations are presented in Supplementary Materials. The results are in line with those previously presented.

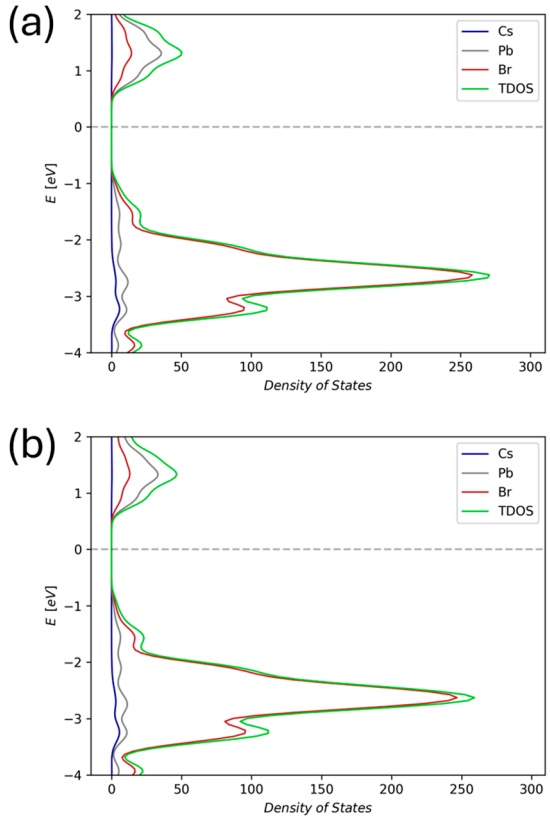

Figure 14. The comparison of the Density of State calculated for $CsPbBr_3$ cubic structure was extracted from crystallographic data (**a**) and calculated using the star point $CsPbI_3$ structure (**b**).

For the initial structures of $CsPbBr_3$ and $CsPbI_3$, the calculated shape of the valence band maximum (VBM) and conduction band minimum (CBM) agrees with the expectations. For all the DOSs calculated for all the structures, it has been noted that VBM consists primarily of the PDOS of halides, and CBM consists primarily of the Pb atom.

4. Conclusions

This paper focuses on the study of $CsPbBr_xI_{3-x}$ perovskites, in particular the influence of halogen type and composition on unit cell parameters as well as the shape of VBM and CBM. The paper consists of two parts: experimental and theoretical.

As for the unit cell parameters, in the experimental part, SEM pictures and XRD measurements were taken for samples with different iodine content with CsBr layers overlaid. Based on the SEM images, it was observed that when the CsBr layer was deposited, the formation of crystals for the sample with a specific iodine content was observed. The SEM results were compared with the diffraction patterns.

Based on the SEM photos, the analysis of the XRD diffraction patterns, and the transmittance graphs, it can be seen that the transition from the initial phases originating from.

$PbBr_2$ + PbI_2 to the perovskite phase takes place for the third and fourth superimposed CsBr layers. Moreover, based on the XRD measurements, the parameters of the unit cell a, b, and c were determined. Unit cell parameters, so a, b, and c, and unit cell volume V were calculated using DFT methods. The results for a, b, and c obtained from the diffraction patterns agree with those calculated with the DFT methods. Moreover, for the results of both the experiment and the calculations, it was noticed that with the increase in the iodine content, the parameters of the unit cell also increased.

Due to the increasing diversity of methods to synthesize perovskites with different compositions, it is worth mentioning other papers describing various methods of synthesis.

An interesting approach to perovskite synthesis is presented by Zheng Chen et al. in the publication "A Confined Fabrication of Perovskite Quantum Dots in Oriented MOF Thin Film" [19]. This approach, in recent years, has become more and more popular for some time and allows one to obtain uniform perovskites [20–22]. It is very likely that MOF Thin Film methods allow one to synthesize more uniform and more repetitive samples than the spin coating method. Nevertheless, the main focus of this paper was not to refine the spin coating method, but to investigate the influence of composition on band structure.

The second part of the publication focuses on the analysis of the influence of iodine on the energy gap value and the shape of the DOS. The experimental value of the energy gap was determined based on the UV-VIS spectra from the Tauc method. As expected, the energy gap value decreased along with the increase in iodine value. The DOS state densities were determined based on the DFT calculations. Here, too, the expected results were reproduced. The gap between CBM and VBM decreases with increasing iodine content. Moreover, the calculations reflected the composition of CBM and VBM. The calculations also showed, as expected, that lead Pb had the major share in CBM, and the halide had the major share in VBM.

To sum up, the results of the experiment and calculations agree with the experimentally determined quantities. Moreover, as expected, the addition of iodine affects the unit cell parameters and the energy gap value. With an increase in the iodine content in a unit cell, the parameters a, b, and c and the volume V increase, and the energy gap decreases.

Supplementary Materials: The following supporting information can be downloaded at https://www.mdpi.com/article/10.3390/physchem5010003/s1, Figure S1: The Density of States for the calculated structure using the protocol with starting point as a cubic structure of $CsPbBr_3$: (a) $CsPbBr_3$; (b) $CsPbBr_2I$; (c) $CsPbBrI_2$; Figure S2: The comparison of the Density of State calculated for $CsPbI_3$ cubic structure was extracted from crystallographic data (a) and calculated using the star point $CsPbBr_3$ structure (b).

Author Contributions: Investigation, A.M., Z.S., M.L. and M.Z.B.; Conceptualization, A.M., Z.S., M.L. and M.Z.B.; Methodology, Z.S., M.L., M.J.W., T.N. and M.Z.B.; Data Analysis, A.M., Z.S. and M.Z.B.; Writing—Original Draft Preparation, A.M.; Writing—Review and Editing, A.M., Z.S., M.L., M.J.W., T.N. and M.Z.B.; funding acquisition, M.L. and T.N.; Supervision, M.Z.B. All authors have read and agreed to the published version of the manuscript.

Funding: This research was funded by the National Science Centre of Poland, Grant Number 2018/31/B/ST8/03294.

Data Availability Statement: Data are contained within the article and Supplementary Materials.

Acknowledgments: We gratefully acknowledge Polish high-performance computing infrastructure PLGrid (HPC Center: ACK Cyfronet AGH) for providing computer facilities and support within computational grant no. PLG/2024/017663. This work was supported by MEXT as "Program for Promoting Research on the Supercomputer Fugaku" (Realization of innovative light energy conversion materials utilizing the supercomputer Fugaku, Grant Number JPMXP1020210317) and FOCUS Establishing Supercomputing Center of Excellence (Japan).

Conflicts of Interest: The authors declare no conflict of interest.

References

1. Victoria, M.; Haegel, N.; Peters, I.M.; Sinton, R.; Jäger-Waldau, A.; del Cañizo, C.; Breyer, C.; Stocks, M.; Blakers, A.; Kaizuka, I.; et al. Solar photovoltaics is ready to power a sustainable future. *Joule* **2021**, *5*, 1041–1056. [CrossRef]
2. Tan, W.H.; Mohamad-Saleh, J. Critical Review on Interrelationship of Electro-Devices in PV Solar Systems with Their Evolution and Future Prospects for MPPT Applications. *Energies* **2023**, *16*, 850. [CrossRef]
3. Blakers, A.; Zin, N.; McIntosh, K.R.; Fong, K. High Efficiency Silicon Solar Cells. *Energy Procedia* **2013**, *33*, 1–10. [CrossRef]

4. Lee, Y.J.; Kim, B.S.; Ifitiquar, S.M.; Park, C.; Yi, J. Silicon solar cells: Past, present and the future. *J. Korean Phys. Soc.* **2014**, *65*, 355–361. [CrossRef]
5. Riede, M.; Spoltore, D.; Leo, K. Organic Solar Cells—The Path to Commercial Success. *Adv. Energy Mater.* **2020**, *11*, 2002653. [CrossRef]
6. Zhou, D.; Zhou, T.; Tian, Y.; Zhu, X.; Tu, Y. Perovskite-Based Solar Cells: Materials, Methods, and Future Perspectives. *J. Nanomater.* **2018**, *2018*, 8148072. [CrossRef]
7. Zhang, J.; Hodes, G.; Jin, Z.; Liu, S. All-Inorganic CsPbBr3 Perovskite Solar Cells: Progress and Prospects. *J. Ger. Chem. Soc.* **2019**, *58*, 15596–15618.
8. Sato, T.; Takagi, S.; Deledda, S.; Hauback, B.C.; Orimo, S.I. Extending the applicability of the Goldshmidt tolerance factor to arbitrary ionic compounds. *Nat. Sci. Rep.* **2016**, *6*, 2359.
9. Li, Z.; Yang, M.; Park, J.S.; Wei, S.H.; Berry, J.J.; Zhu, K. Stabilizing Perovskite Structures by Tuning Tolerance Factor: Formation of Formamidinium and Cesium Lead Iodide Solid-State Alloys. *Chem. Mater.* **2016**, *28*, 284–292. [CrossRef]
10. Bartel, C.J.; Sutton, C.; Goldsmith, B.R.; Ouyang, R.; Musgrave, C.B.; Ghiringhelli, L.M.; Scheffler, M. New tolerance factor to predict the stability of perovskite oxides and halides. *Sci. Adv.* **2019**, *5*, eaav0693. [CrossRef]
11. Zhang, W.; Liu, X.; He, B.; Zhu, J.; Li, X.; Shen, K.; Chen, H.; Duan, Y.; Tang, Q. Enhanced Efficiency of Air-Stable $CsPbBr_3$ Perovskite Solar Cells by Defect Dual Passivation and Grain Size Enlargement with a Multifunctional Additive. *Appl. Mater. Interfaces* **2020**, *12*, 36092–36101. [CrossRef] [PubMed]
12. Hoffman, J.B.; Schleper, A.L.; Kamat, P.V. Transformation of Sintered $CsPbBr_3$ Nanocrystals to Cubic $CsPbI_3$ and Gradient $CsPbBrxI_{3-x}$ through Halide Exchange. *J. Am. Chem. Soc.* **2016**, *138*, 8603–8611. [CrossRef] [PubMed]
13. Li, Z.; Jin, Z. HI hydrolysis-derived intermediate as booster for CsPbI3 perovskite: From crystal structure, film fabrication to device performance. *J. Semicond.* **2020**, *41*, 051202. [CrossRef]
14. Jiang, M.; Hu, Z.; Ono, L.K.; Qi, Y. $CsPbBr_xI_{3-x}$ thin films with multiple ammonium ligands for low turn-on pure-red perovskite light-emitting diodes. *Nano Res.* **2020**, *14*, 191–197. [CrossRef]
15. Perdew, J.P.; Burke, K.; Ernzerhof, M. Generalized gradient approximation made simple. *Phys. Rev. Lett.* **1996**, *77*, 3865–3868. [CrossRef] [PubMed]
16. Grimme, S. Semiempirical GGA-type density functional constructed with a long-range dispersion correction. *J. Comput. Chem.* **2006**, *27*, 1787–1799. [CrossRef]
17. Kühne, T.D.; Iannuzzi, M.; Del Ben, M.; Rybkin, V.V.; Seewald, P.; Stein, F.; Laino, T.; Khaliullin, R.Z.; Schütt, O.; Schiffmann, F.; et al. CP2K: An electronic structure and molecular dynamics software package—Quickstep: Efficient and accurate electronic structure calculations. *J. Chem. Phys.* **2020**, *152*, 194103. [CrossRef] [PubMed]
18. Hutter, J.; Iannuzzi, M.; Schiffmann, F.; VandeVondele, J. CP2K: Atomistic simulations of condensed matter systems. *WIREs Comput. Mol. Sci.* **2014**, *4*, 15–25. [CrossRef]
19. Chen, Z.; Gu, Z.; Fu, W.; Wang, F.; Zhang, J. A Confined Fabrication of Perovskite Quantum Dots in Oriented MOF Thin Film. *ACS Appl. Mater. Interfaces* **2016**, *8*, 28737–28742. [CrossRef]
20. Li, Z.; Yu, C.; Wen, Y.; Wei, Z.; Chu, J.; Xing, X.; Zhang, X.; Hu, M.; He, M. MOF-Confined Sub-2 nm Stable $CsPbX_3$ Perovskite Quantum Dots. *Nanomaterials* **2019**, *9*, 1147. [CrossRef]
21. Shu, B.; Chang, Y.; Dong, L.; Chen, L.; Wang, H.; Yang, S.; Zhang, J.; Cheng, X.; Yu, D. Highly stable $CsPbBr_3$ perovskite dots incorporated in aliminum stearate. *J. Lumin.* **2021**, *234*, 117962. [CrossRef]
22. Protesescu, L.; Calbo, J.; Williams, K.; Tisdale, W.; Walsh, A.; Dincă, M. Colloidal nano-MOFs nucleato and stabilize ultra-small quantum dots of lead bromide perovskites. *Chem. Sci.* **2021**, *12*, 6129–6135. [CrossRef] [PubMed]